A Complete High-Resolution Coastline of Antarctica Extracted from Orthorectified Radarsat SAR Imagery

Hongxing Liu and Kenneth C. Jezek

Abstract

A complete, high-resolution coastline of Antarctica, extracted from an orthorectified mosaic of Radarsat-1 synthetic aperture radar (SAR) images through a sequence of automated image processing algorithms, is presented. A locally adaptive thresholding method is used to segment the orthorectified SAR images, while image-object formation and labeling, and edge-tracing techniques are used to process the segmented images into vector-based cartographic products of coastline, defined here as the boundary between continental ice or rock exposures and sea ice covered ocean. The absolute accuracy of planimetric positioning of the resultant coastline is estimated to better than 130 m, and its spatial resolution (25 m) is adequate for supporting cartographic and scientific applications at 1:50,000 scale. This radar-image-derived coastline gives an accurate description of geometric shape and glaciological characteristics of the Antarctic coasts and also provides a precise benchmark for future change-detection studies.

Introduction

Coastline delineation is a prerequisite for the geographic description of the physical form of a continent. This seemingly simple task was still unfinished for the Antarctic continent until recently (Fox and Cooper, 1994). Some portions of the Antarctic coast have never been accurately mapped, and other portions have experienced dramatic changes in positions and shapes since they were mapped. Information about geographic position, orientation, and geometric shape of the Antarctic coastline is essential for geographic exploration, and nautical and aerial navigation. In addition, the area and volume of the Antarctic Ice Sheet are intricately linked to global climate, and changes in the shape and extent of the ice sheet may be diagnostic indicators of changing climate (Mercer, 1978; Williams and Hall, 1993). Constructing an accurate coastline map is an important step toward establishing a baseline for future change detection studies in order to understand the response of the Antarctic Ice Sheet to climate change.

In this paper, we present a complete high-resolution Antarctic coastline, which we define as the boundary between the ocean and the continental ice sheet, including ice shelves and coastal rock outcrops. The coastline is extracted from 1997 Radarsat-1 synthetic aperture radar (SAR) image mosaic. The mosaic is compiled from individual SAR image frames that have undergone rigorous terrain correction, geocoding, and radiometric correction and balancing, and therefore furnishes a planimetrically accurate image base for interpreting and delineating coastline features. A chain of image processing algorithms has been applied to the orthorectified images to automate the coastline extraction. The final coastline products in ArcInfo vector line coverage format will be provided to the National Snow and Ice Data Center and to the British Antarctic Survey for eventual distribution to the science community. We believe that this highly accurate coastline will be useful for a wide range of cartographic and scientific applications.

In the following sections, we will first give an overview of the image data and summarize the techniques used to create the orthorectified SAR image mosaic. Then we describe our automated coastline extraction algorithms. Next, the relative and absolute accuracy of the extracted coastline is evaluated, and the shape property of the coastline is also analyzed. In the final section, we draw some conclusions.

Image Data Source and Methodology Overview

Antarctica is the coldest, windiest, and, on average, highest continent on Earth. The size of Antarctica approximates the areas of the United States and Mexico combined. The continent was first sighted in 1819, and the first landing was made in 1821 (Larsgaard, 1993). The harsh climate, inaccessibility, and long dark winters imposed serious difficulties and challenges on the conventional surveying and mapping techniques. By the end of the Second World War, more than half of the Antarctic coastline was still uncharted, and the interior was largely blank (Larsgaard, 1993). At present, the larger-scale maps (1:250,000 or larger) only cover portions of Antarctica, including the Antarctic Peninsula, Transantarctic Mountains, and parts of Dronning Maud Land and Marie Byrd Land, while most parts of the continent remain poorly mapped at 1:1,000,000 or smaller scale. Severe geolocation errors of up to 30 km have been observed and reported in the existing maps (Larsgaard, 1993; Williams *et al.*, 1995; Jezek *et al.*, 2000).

Satellite remote sensing technology overcomes the obstacles of surface travel and provides an efficient means for mapping the Antarctic continent. Optical satellite sensors, especially AVHRR and Landsat, have been used extensively in mapping and studying Antarctic continent since the late 1970s (Swithinbank, 1988; Williams *et al.*, 1995; Ferrigno *et al.*, 1996; Mullins *et al.*, 1999). However, optical sensors are affected by clouds, and images are often saturated due to the

H. Liu is with the Department of Geography, Texas A&M University, College Station, TX 77843 (liu@geog.tamu.edu).

K.C. Jezek is with the Byrd Polar Research Center, The Ohio State University, Columbus, OH 43210 (jezek@frosty.mps.ohio-state.edu).

Photogrammetric Engineering & Remote Sensing
Vol. 70, No. 5, May 2004, pp. 605–616.

0099-1112/04/7005–0605/$3.00/0

high albedo of snow for visible wavelengths. With abilities to peer through clouds and to observe day and night, spaceborne radar sensors provide ideal instruments for mapping the Antarctic continent. In 1997, a major milestone was reached in Antarctic mapping history when the entire Antarctic continent was imaged over 30 days by the Canadian Radarsat-1 SAR sensor during the first Antarctic Imaging Campaign (AIC-1), as a part of the NASA pathfinder project-Radarsat Antarctic Mapping Project (RAMP). Based on the SAR images, a seamless image mosaic has been produced at the Byrd Polar Research Center of The Ohio State University (Jezek 1999). In 2000, the entire Antarctic continent was imaged again by the Radarsat-1 SAR sensor during the second Antarctic Imaging Campaign (AIC-2) (Jezek, 2002). The second SAR image mosaic is being processed at the Byrd Polar Research Center.

Our present analysis is based on the radar image mosaic compiled from data that were acquired by the Canadian satellite Radarsat-1 using C-band (5.6-cm wavelength) SAR sensor at a 25-m resolution from 09 September to 20 October, 1997 (Jezek, 1999). The imaging period was selected to minimize complications associated with snowmelt conditions near the margin of the Antarctic ice sheet. The coastal regions were imaged mainly using the standard beam 2 with a nominal incidence angle (look angle) of 24° to 31°. During the mission, Radarsat-1 was maneuvered in orbit to rotate the normally right-looking SAR to a left-looking mode to image the interior of the Antarctic for the first time. The combination of over 4000 SAR image frames collected over 30 days provides a near instantaneous, high-resolution view of the entire Antarctic continent and offshore ocean. Those images are ideal sources for deriving a consistent, high-resolution coastline for Antarctica.

Although radar imagery is not affected by clouds, there are still some difficulties and problems associated with coastline detection and delineation (Lee and Jurkevich, 1990; Mason and Davenport, 1996). Apart from the presence of speckle, radar imagery contains inherent geometric and terrain distortions due to its side-looking geometry. To attain the geometric fidelity of the derived coastline, the SAR imagery must be orthorectified to remove the severe geometric distortions. To achieve a complete and consistent coastline coverage, it is also desirable to precisely geocode, radiometrically balance, and then merge individual SAR images into a mosaic prior to coastline extraction operations.

Under cloud-free weather conditions, optical satellite imagery with near-infrared bands commonly provides sufficient contrast between land and water for delineating the coastline (Ryan *et al.*, 1991). However, the intensity contrast between land and sea on a radar image is greatly dependent on wind and sea ice conditions (Lee and Jurkevich, 1990; Mason and Davenport, 1996). If there is little or no wind, the ocean water appears clearly darker than the land in a radar image. In the case of strong wind, the radar signal return from the wind-roughened and wave-modulated water surfaces can equal or exceed the return from a nearby land area, resulting in an inadequate contrast for unambiguous separation between ocean water and landmass. In addition, radar signals return from rock outcrops, dry snow, bare ice, and topography-induced radar shadows may be similar to or even weaker than those from ocean water. Furthermore, the presence of sea ice and icebergs in the surrounding oceans of Antarctica further complicates the automated coastline extraction. For these reasons, most general-purpose edge detection and image segmentation techniques are inadequate for the purpose of automated coastline extraction (Lee and Jurkevich, 1990; Ryan *et al.*, 1991; Mason and Davenport, 1996; Sohn and Jezek, 1999).

In this research, we developed a comprehensive technique for maximizing automation of the coastline extraction process. A functional block diagram of our coastline extraction method is shown in Figure 1. As part of the Radarsat Antarctic Mapping Project, the SAR images are orthorectified and mosaicked to remove geometric and terrain distortions and to assign precise geographic coordinates to image pixels. Then, a sequence of image processing algorithms is applied to the orthorectified SAR mosaic to automate the coastline extraction. These algorithms are organized to perform three consecutive operations: preprocessing, segmentation, and postprocessing. At the preprocessing stage, a Lee filter and an anisotropic diffusion operator are used to suppress speckle noise and to enhance the coastline edges. At the segmentation stage, a locally adaptive thresholding method is used to segment the SAR images into homogeneous ice/land and water regions, at which point the Levenberg-Marquardt method is introduced to fit the bimodal Gaussain parameters, and a Canny edge detector is used to refine the observed histogram and to estimate reliable initial values for the bimodal Gaussian parameters. At the postprocessing stage, image-object formation and labeling, removal of noisy image objects, edge tracing, and vectorization algorithms are sequentially applied to the segmented images for extracting a vector representation of coastlines. Within the ArcInfo GIS environment, the sections of the coastline extracted from individual images are further edited for possible errors and consistent orientation, and are merged into a single complete ArcInfo vector line coverage.

Orthorectification of SAR Imagery

The geographic position and geometric shape of the derived coastline are inherited from the SAR imagery. To obtain a coastline with a precise location and reliable geometric shape, the source SAR images need to be orthorectified and map projected. Adhering to the recommendations of Scientific Committee of Antarctic Research (SCAR), we choose the Polar Stereographic projection as the standard map projection for orthorectification, and consequently the derived coastline products are also in the same projection. The key parameters of this projection are listed in Table 1.

The processing procedure for orthorectification consists of four major components: block bundle adjustment, terrain correction and geocoding, radiometric correction and balancing, and mosaicking. These basic operations are performed with the Radarsat Antarctic Mapping System (RAMS) developed by the Vexcel Corporation (Norikane *et al.*, 1996).

Block Bundle Adjustment

Precise knowledge of the sensor position is crucial for associating image coordinates (pixel row and column number) to absolute geographical locations on the ground (polar stereographic coordinates). Due to the uncertainty in the Radarsat spacecraft ephemeris, the raw error for geolocating a ground target is on the order of about 200 m (Jezek and Carsey, 1993). In order to improve the geocoding accuracy, a block bundle adjustment procedure is used to refine the satellite ephemeris information. Each block consists of a group of satellite orbits

TABLE 1. PARAMETERS FOR THE POLAR STEREOGRAPHIC PROJECTION IN ANTARCTICA

Parameters	Values
Standard parallel	71°S latitude
Central meridian	0° longitude
Origin (0,0)	South Pole
False Easting	0
False Northing	0
Unit	Meter
Reference ellipsoid	WGS84

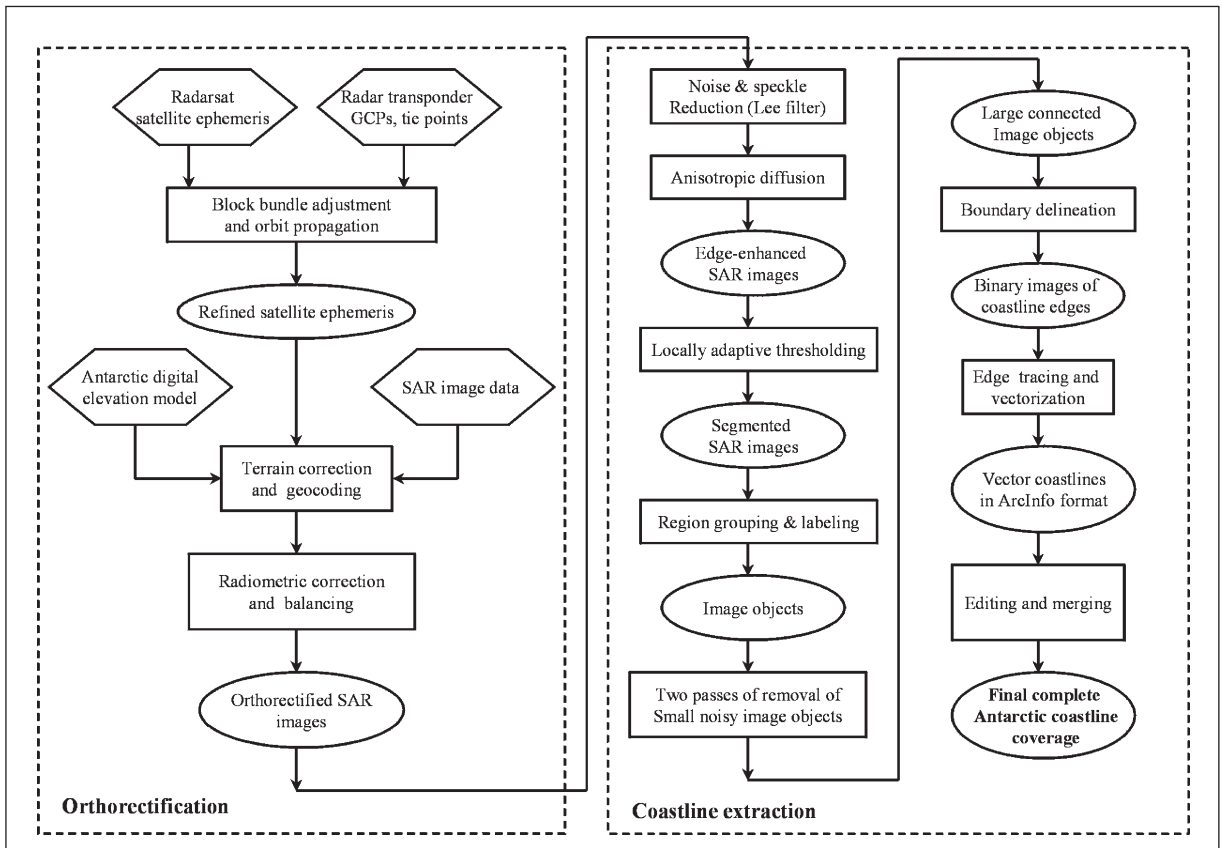

Figure 1. Data flow chart and image processing chain for Antarctic coastline extraction. Hexagons represent input data, rectangles represent a processing step, and ovals represent the resulting data sets.

with approximately 150 to 200 SAR image frames. Recognizable image features are selected over the overlap regions of adjacent orbits as orbit-to-orbit tie points, which are used to perform relative orientation (internal adjustment) of the image frames from one orbit to other orbits in the block.

It was and still is very expensive and difficult to establish stable geodetic control in Antarctica, due to the following reasons: the harsh weather conditions, especially the frequent and often enduring blizzards; the vast expanses of featureless surface; limited rock exposure; and the constant motion of the ice and snow. Fortunately, spaceborne mapping techniques require far fewer ground control points (GCPs) than does conventional aerial photography, owing to the large ground coverage of each satellite image frame, the relative stability and predictability of the satellite orbit, and the block bundle adjustment technique. With the assistance of the Environmental Research Institute of Michigan (ERIM), about 230 GCPs with accuracy on the order of about 25 m were acquired (Jezek, 2002). These GCPs are mainly distributed along the coast where scientific stations, rock outcrops, or nunataks (bedrock that sticks above the surface of an ice sheet) exist (Figure 2). Prior to the first Antarctic Imaging Campaign, a radar transponder was deployed at the South Pole and geolocated using GPS technology. The transponder was operated throughout the mission as a geographic reference point for the Radarsat-1 SAR sensor. Because the satellite observed the South Pole on each orbit, the transponder provided good control for tying different orbits together.

Following establishment of the GCPs and the radar transponder, the absolute orientation (position and velocity vectors) of the SAR sensor was adjusted for a group of orbits that constitutes each block by simultaneously solving a group of radar range and Doppler equations (Curlander *et al.*, 1987; Leberl, 1990; Kwok *et al.*, 1990):

$$R(t) = \sqrt{(\vec{S}(t) - \vec{P}(t))\bullet(\vec{S}(t) - \vec{P}(t))} \quad (1)$$

$$f_D(t) = \frac{2}{\lambda R(t)}(\vec{V}_S(t) - \vec{V}_P(t))\bullet(\vec{S}(t) - \vec{P}(t)) \quad (2)$$

where $\vec{S}(t) = (X_S, Y_S, Z_S)$ and $\vec{V}_S(t) = (\dot{X}_S, \dot{Y}_S, \dot{Z}_S)$ are, respectively, the position and velocity vectors of the sensor to be refined; t is the time when the GCP is imaged; $\vec{P}(t) = (X, Y, Z)$ is the known position of a GCP in the 3D Cartesian coordinate system; $\vec{V}_P(t) = (\dot{X}, \dot{Y}, \dot{Z})$ is the velocity vector of the GCP due to the Earth's rotation; $R(t)$ is the slant range from the sensor to the GCP; $f_D(t)$ is the Doppler frequency shift of the GCP; λ is radar wavelength; and the dot ($\bullet$) denotes the inner product of vectors.

After the above external adjustment, the refined sensor position and velocity vectors at the GCPs are modeled by a polynomial equation in terms of time t, and then repropagated and applied to each orbit, including the orbit segments where no GCPs are available.

Terrain Correction with the Antarctic Digital Elevation Model

Due to the side-looking viewing geometry, geometric distortions in SAR images are much more severe than in optical satellite images. As a range device, the SAR sensor essentially measures the absolute distance (slant range) from the sensor to a ground target. As a result, the features in the near range of the resulting SAR image appear compressed relative to the far range, which is known as slant-range scale distortion. Furthermore, surface topography induces additional local terrain distortions,

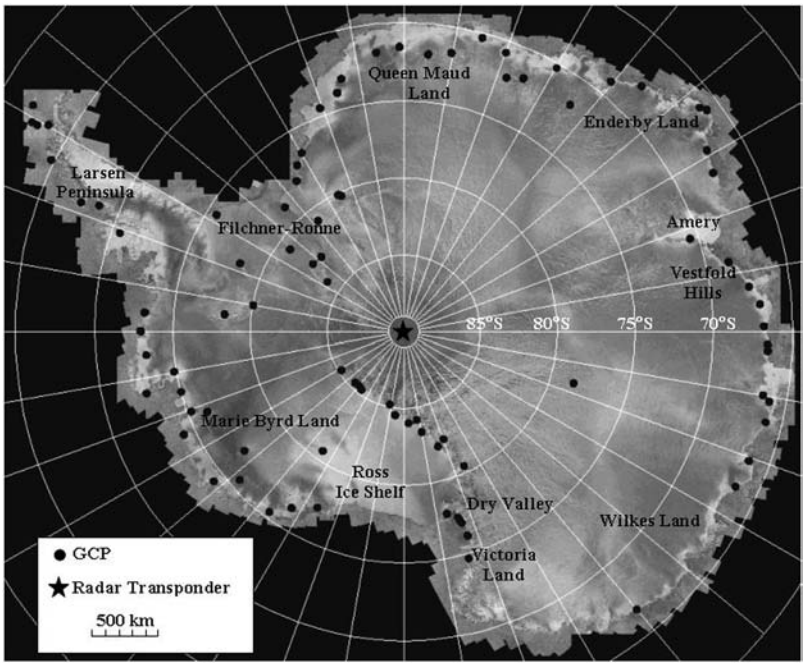

Figure 2. Locations of GCPs and radar transponder on the orthorectified SAR image mosaic.

including foreshortening, layover, and shadowing (Naraghi *et al.*, 1983; Leberl, 1990). The relief displacement toward the radar antenna causes the foreshortening effect, namely, the imaged terrain surface sloping toward the radar antenna (foreslope) appears shortened relative to those sloping away from the radar (backslope). As shown in Figure 3, the radar relief displacement dx in the range direction can be approximated by the following equation (Leberl, 1990; Johnsen *et al.*, 1995):

$$dx \cong -\frac{h}{\tan\theta} \tag{3}$$

where h is the height of position x above the WGS84 reference ellipsoid, and θ is the incidence angle of the radar beam at position x. The average elevation of Antarctica is about 1950 m, which gives a range direction mislocation of about 3,700 m for a Radarsat-1 Standard Beam 2 image.

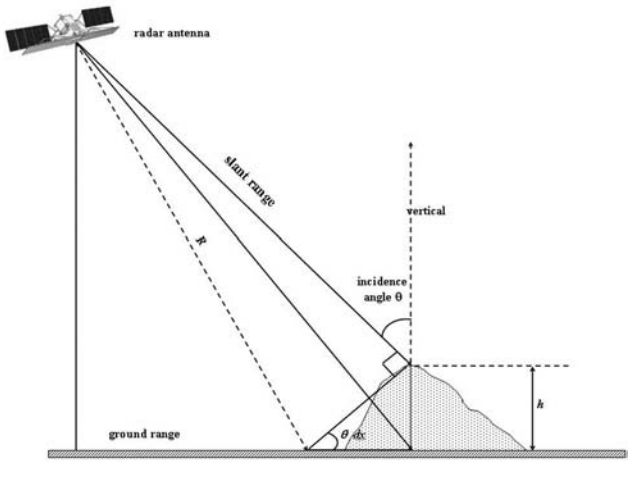

Figure 3. Terrain distortions in a SAR image.

Based on a high-resolution digital elevation model (DEM) of Antarctica (Liu *et al.*, 1999), we corrected terrain distortions in the SAR imagery using the RAMS software package. The elevation model was created by integrating cartographic and remotely sensed data. The accuracy of the DEM is estimated at about 100 to 130 m over the rugged mountainous area, better than 2 m for the ice shelves, better than 15 m for the interior ice sheet, and about 35 m for the steeper ice sheet perimeter (Liu *et al.*, 1999). Layover and radar shadows cannot be corrected with a single SAR image. Instead, layover and radar shadow masks are predicted based on the Antarctic digital elevation model, then are filled up by SAR images acquired from different radar beams (with different incidence angles) or look directions (ascending or descending orbit).

Radiometric Correction and Balancing

Radarsat-1 SAR image sources were radiometrically calibrated at the Alaska SAR facility to relate the digital numbers (DNs) of images to the radar backscattering coefficient σ_0, by applying antenna pattern inversion, differential range attenuation correction, and absolute gain adjustment. Additional radiometric correction was performed through RMPS to adjust the backscatter for the effect that terrain has on the illuminated area. Significant radiometric differences (in units of σ_0) exist between adjacent image frames from different orbits. These arise from several sources, including differences in incidence angles between adjacent frames, temporal variations in SAR backscatter, and artifacts associated with the satellite on-board automatic gain control. To remove and mitigate seams between adjacent orbits, radiometric tie points were selected in the overlap regions, and a least-squares error surface was calculated from these tie points to balance the radiometry and feather the seams (Kwok *et al.*, 1990; Norikane *et al.*, 1996). Figure 4 compares a portion of the SAR image mosaic before and after

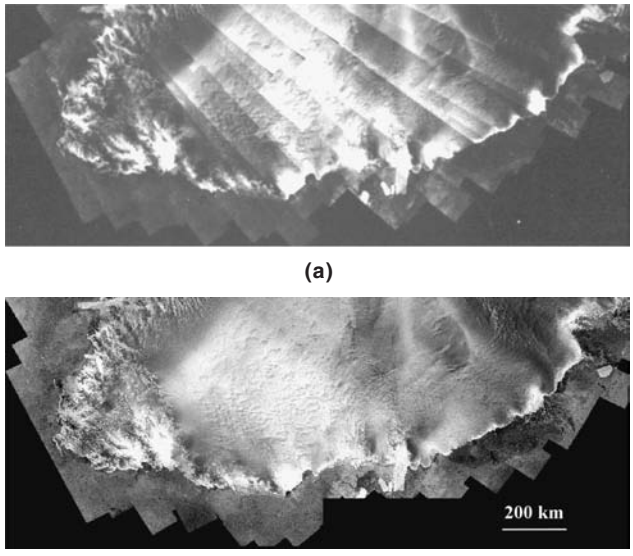

Figure 4. Effect of radiometric correction and balancing. (a) Before radiometric balancing. (b) After radiometric balancing.

radiometric correction and balancing. Radiometric balancing removes the seam lines, and, hence, avoids the complication of differentiating the seam lines from the true coastlines in the subsequent coastline extraction process.

Through the block bundle adjustment, terrain correction, and radiometric correction and balancing, seamless image blocks were created. A final, grand block adjustment was used to register the individual blocks into a final mosaic product. Similarly, a grand radiometric adjustment was applied to remove residual seams between blocks. This resulted in a complete, seamless orthorectified giant SAR image mosaic (Figure 2). Comparison with the reserved checkpoints and GPS data shows that the absolute geolocation accuracy of the SAR image mosaic is about 50 to 100 meters. This precisely geocoded and terrain corrected image mosaic warrants the fidelity of the geometric shapes and the accuracy of the absolute geographic position of the derived coastline.

Automated Coastline Extraction Algorithms

Because of the size of the resulting product, the SAR mosaic is subsetted into separate image tiles. Each coastal image tile is processed using an automated coastline extraction procedure (Figure 1), which consists of three consecutive processing stages: preprocessing, segmentation, and postprocessing. We have implemented the algorithms using C programming language.

Image Preprocessing with Lee Filter and Anisotropic Diffusion Operator

The preprocessing algorithms aim to suppress image noise and speckle, and enhance coastline edge elements in the images. Speckle is a grainy salt-and-pepper noise (random bright and dark pixels) in radar imagery that is present due to random constructive and destructive interference of coherent radar waves. An edge-preserving filter, the Lee filter (Lee, 1986) with a 5 by 5 window, is applied to each image tile for filtering radar speckle without blurring the coastline edges.

We also utilize an anisotropic diffusion algorithm (Perona and Malik, 1990; Saint-Marc *et al.*, 1991; Sohn and Jezek, 1999), which is an efficient non-linear technique for suppressing image noise and unwanted edges. Based on a four-neighborhood window, the anisotropic diffusion operator computes the diffused pixel value in an iterative fashion using the following equation:

$$I_{i,j}^{t+1} = I_{i,j}^{t} + \lambda[c_{i-1,j}\nabla I_{i-1,j} + c_{i+1,j}\nabla I_{i+1,j} + c_{i,j-1}\nabla I_{i,j-1} + c_{i,j+1}\nabla I_{i,j+1}] \quad (4)$$

where $I_{i,j}^{t+1}$ is the new value of the central pixel at the $t+1$ iteration, $I_{i,j}^{t}$ is the value of the central pixel at the t iteration, λ is the weight value, and $\nabla I_{i,j}$ is the four-neighbor gray-level difference (gradients). The gradient $\nabla I_{i,j}$ is computed between the central processing pixel and its four immediate neighbors:

$$\begin{cases} \nabla I_{i-1,j} = I_{i-1,j} - I_{i,j} \\ \nabla I_{i,j-1} = I_{i,j-1} - I_{i,j} \\ \nabla I_{i+1,j} = I_{i+1,j} - I_{i,j} \\ \nabla I_{i,j+1} = I_{i,j+1} - I_{i,j} \end{cases}. \quad (5)$$

The above gradients are used to compute the directional diffusion coefficients $c_{m,n}$:

$$c_{m,n} = \frac{1}{1 + \left(\frac{\|\nabla I_{m,n}\|}{K}\right)^2}; \qquad (m=i-1,i,i+1;\ n=j-1,j,j+1;\ m \neq n) \quad (6)$$

where K is the gradient threshold. The edges with a gradient higher than K are enhanced, while unimportant edges with a weaker gradient than K are suppressed.

Through experiments, we determined that the following parameter values are appropriate for our SAR image data: $\lambda = 0.25$, $K = 8$, and iteration $= 5$. The anisotropic diffusion retains and enhances strong edges (with a gradient greater than 8) along the coastline while smoothing weak edges (with a gradient smaller than 8) and interior intensity variations inside the land and ocean masses (see Figures 6a and 6b). This effectively reduces the noisy image objects and hence false edges at the following image segmentation stage.

Image Segmentation with Locally Adaptive Thresholding Algorithm

The purpose of image segmentation is to separate a SAR image into its constituent homogeneous image regions, which define the boundaries between ice/land and ocean masses. In order to reliably separate ice/land pixels from water pixels, we developed a locally adaptive thresholding algorithm for image segmentation.

For a small image region consisting of ice/land and water pixels, intensity values tend to be grouped into two dominant modes (lobes) with relatively distinct mean values. As shown in Figure 5, the overall histogram generally exhibits a bimodal shape, namely, two peaks and a valley. We assume that the bimodal distribution is a mixture of two Gaussian (normal) distribution functions. The probability density function $p(x)$ of the bimodal image region is modeled by Equation 7 with five unknown parameters (Chow and Kaneko, 1972; Haverkamp *et al.*, 1995): i.e.,

$$p(x) = \frac{p_1}{\sqrt{2\pi}\sigma_1}\exp\left[-\frac{(x-\mu_1)^2}{2\sigma_1^2}\right] + \frac{1-p_1}{\sqrt{2\pi}\sigma_2}\exp\left[-\frac{(x-\mu_2)^2}{2\sigma_2^2}\right] \quad (7)$$

where μ_1 and μ_2 are the mean values of two component normal distributions, σ_1 and σ_2 are the standard deviations about the means, and p_1 is the coefficient of the mixture, representing the theoretical fraction of area occupied by water (background) pixels in the image region.

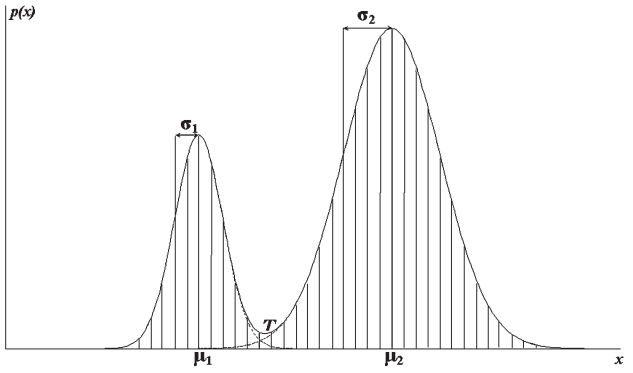

Figure 5. Bimodal shape of histogram and five-parameter Gaussian curve fitting.

We utilize the Levenberg-Marquardt method (Press *et al.*, 1992) for iteratively fitting the five parameters for non-linear bimodal Gaussian curve given by Equation 7. To improve the fitting quality and speed up the convergence of the iterative process, the mixed (edge) pixels detected by the Canny edge detector (Canny, 1986; Parker, 1997) are removed from the formation of observed histogram, and the mixed (edge) pixels and their immediate neighboring pixels along two sides are used to calculate the initial estimates of bimodal Gaussian parameters (Liu and Jezek, 2004). For most image regions, the convergence for the Levenberg-Marquardt algorithm can be achieved within four to seven iterations.

For an image region whose histogram has appreciable bimodality and passed the bimodality test (Chow and Kaneko, 1972, Liu and Jezek, 2004), the optimal threshold value T (the valley point in the histogram) is analytically computed based on the five Gaussian parameters. The optimal threshold value T is so defined that all pixels with an intensity value below T are considered water pixels and all pixels with an intensity value above T are considered land pixels. The probability of erroneously classifying a land pixel as a water pixel is

$$E_1(T) = \int_{-\infty}^{T} \frac{1}{\sqrt{2\pi}\sigma_2} \exp\left[-\frac{(x-\mu_2)^2}{2\sigma_2^2}\right] dx. \quad (8)$$

Similarly, the probability of erroneously classifying a water pixel as a land pixel is

$$E_2(T) = \int_{T}^{\infty} \frac{1}{\sqrt{2\pi}\sigma_1} \exp\left[-\frac{(x-\mu_1)^2}{2\sigma_1^2}\right] dx. \quad (9)$$

The overall probability of the classification error is

$$E(T) = (1 - p_1)E_1(T) + p_1E_2(T). \quad (10)$$

The requirement for minimizing the probability of misclassification is given by Equation 11:

$$\frac{\partial E(T)}{\partial T} = (1 - p_1)\frac{\partial E_1(T)}{\partial T} + p_1\frac{\partial E_2(T)}{\partial T} = 0. \quad (11)$$

Substituting Equations 8 and 9 into Equation 11 and applying Liebnitz's rule, we obtain

$$\frac{(1 - p_1)}{\sigma_1} \exp\left[-\frac{(T - \mu_1)^2}{2\sigma_1^2}\right] = \frac{p_1}{\sigma_2} \exp\left[-\frac{(T - \mu_2)^2}{2\sigma_2^2}\right]. \quad (12)$$

From Equation 12, we can derive the optimal threshold T:

$$T = \frac{-B \pm \sqrt{B^2 - 4AC}}{2A} \quad (13)$$

where

$$A = \sigma_1^2 - \sigma_2^2,$$

$$B = 2\left(\mu_1\sigma_2^2 - \mu_2\sigma_1^2\right), \text{ and}$$

$$C = \sigma_1^2\,\mu_2^2 - \sigma_2^2\,\mu_1^2 + 2\sigma_1^2\sigma_2^2 \ln\frac{\sigma_2 p_1}{\sigma_1(1 - p_1)}.$$

One of two possible solutions for T can trivially be dropped by checking the condition $\mu_1 < T < \mu_2$.

In our analysis, a predefined portion (an image tile) of the SAR image is divided into an array of overlapping image blocks. There is a 50 percent overlap between adjacent image blocks. Image blocks that have a high intensity variance value are selected for fitting a bimodal Gaussian curve and determining the optimal threshold. The processing of the selected image blocks results in a set of irregularly distributed thresholds. For uniform blocks with a small intensity variance, their local threshold values are determined by an inverse distance weighted (IDW) interpolation method (Liu and Jezek, 2004). Subsequently, we segment the entire image into a binary image, consisting of land and water pixels. Those with an intensity value below their local threshold are flagged as water pixels, and others with an intensity value above their local threshold are designated as land pixels.

The relative positional accuracy of the extracted coastline depends on the performance of the image segmentation algorithm, which in turn depends upon the reliability and correctness of the local threshold. Because our thresholding method sets the threshold value dynamically according to the local image statistical properties, a good separation between the ice/land and ocean water is achieved (Figure 6). If a single global threshold were used for the entire image to determine the ice/land and water boundaries, some local coastline edges would have remained undetected due to the heterogeneity of the intensity contrast, causing the discontinuity of coastline edges in low contrast areas and inconsistency of coastline edge position between high contrast and low contrast areas.

Postprocessing of Segmented Images

After segmentation, image pixels are classified into two categories: ice/land (object) and water (background) pixels. In order to correct misclassifications, to differentiate the coastline edges from other object edges, and to vectorize the raster-based coastline edge pixels, several postprocessing algorithms are applied to the segmented images.

In the segmented image, an image region formed by a set of spatially connected ice/land pixels is presumed to define a homogeneous mass. Similarly, a region formed by connected water pixels is expected to define a homogeneous ocean mass. However, misclassifications are present due to the complexity of the received radar signal. For example, fast ice, new and first year sea ice, and icebergs in the ocean are often misclassified as glacier ice pixels. Rock outcrops, dry snow, refrozen lakes, and radar shadows in high relief areas tend to be classified as water pixels. The primary characteristic of these misclassified pixels is that the areal size of the image region formed by these misclassified pixels is significantly smaller than that of true ice/land or ocean image regions. This characteristic is utilized in the post processing to correct the misclassification.

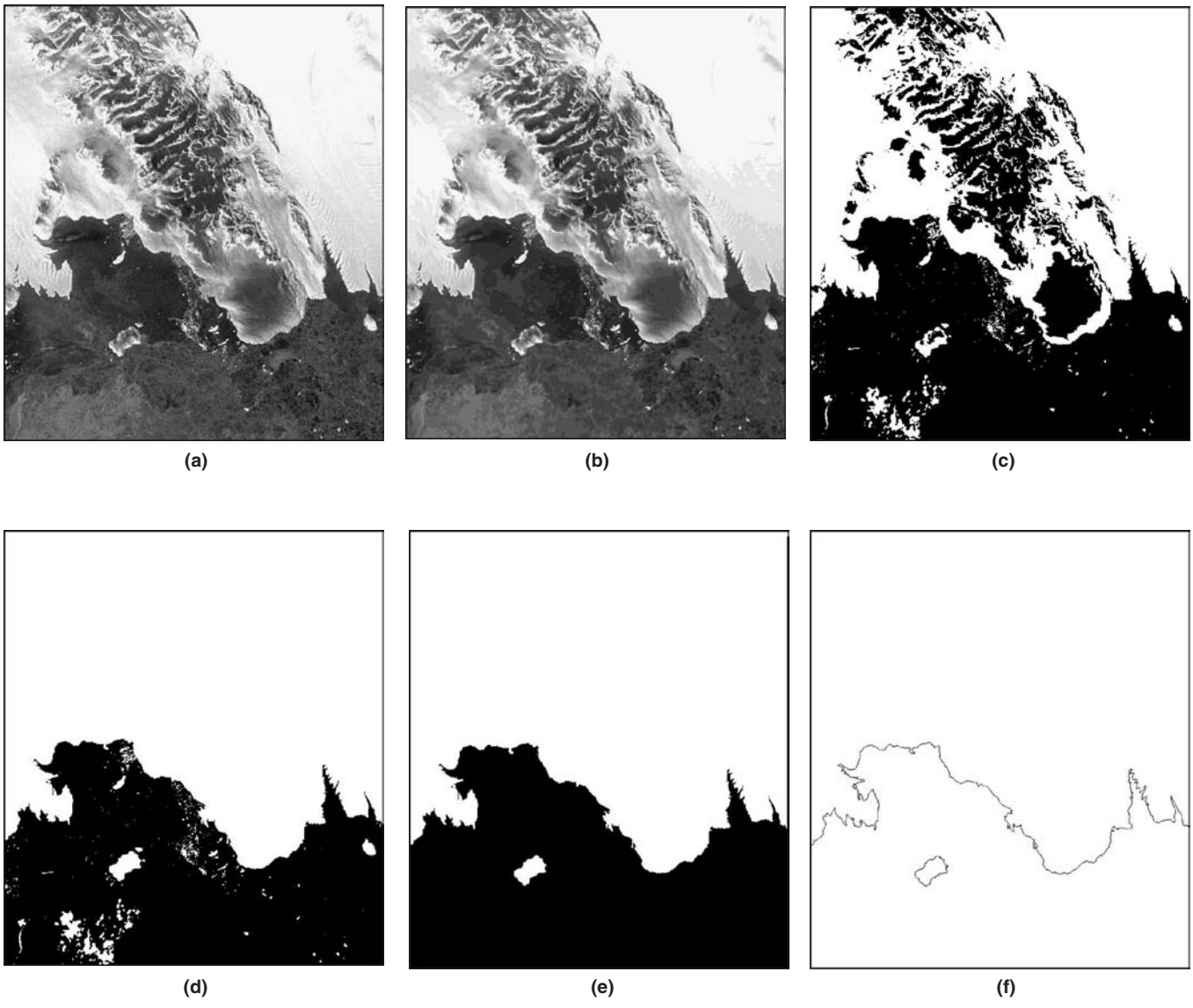

Figure 6. Image segmentation and post-processing. (a) Input SAR image. (b) SAR image after applying Lee filter and anisotropic diffusion. (c) Segmented image by the locally adaptive thresholding algorithm. (d) Removal of small noisy water image objects. (e) Removal of small noisy land image objects. (f) Extracted vector coastline.

The postprocessing procedure goes as follows. First, individual water regions (connected water pixels) are identified to form water objects by a recursive "grassfire" algorithm (Liu and Jezek, 2004). Each image object is labeled with an identification number, and its areal size is also calculated during the image object formation and labeling process. With a user specified areal threshold, small water objects corresponding to rock outcrops, dry snow zones, frozen lakes, and radar shadows are removed by changing them into ice/land pixels (Figure 6d). In the second pass of processing, individual ice/land objects are identified and labeled using the same algorithm. Relatively small ice/land objects corresponding to sea ice, icebergs, and small islands are removed by changing them into water pixels. After two passes of selective removal of small, isolated, and noisy image objects, only large continuous ice/land and ocean image objects are left, which define the true ice/land and water boundary (Figure 6e).

The ice/land pixels immediately adjacent to the ocean water pixels are delineated by a 3 by 3 neighborhood operator as the coastline edge pixels. Then, the extracted coastline pixels are traced using a robust recursive edge-tracing algorithm (Liu and Jezek, 2004). Their coordinates are recorded into a vector-based ArcInfo Ungenerate file, which is loaded into ArcInfo software to generate a vector coverage of the coastline (Figure 6f).

Editing and Merging Coastline Segments

By applying the above sequence of image processing algorithms, the coastline is automatically extracted from each image tile. Despite its overall accuracy, some delineation

errors were detected during the batch processing of image tiles. One type of error occurs in extensive fast ice (sea ice welded to either the coastal ice sheet or rock). Here, the backscatter difference between glacier ice and fast ice is smaller than the contrast between ocean and fast ice. The other error occurs when rock outcrops or dry snow are adjacent to smooth ocean water, resulting in artificial inlets or false openings over the rock outcrops or dry snow region. These errors are sporadic and infrequent, and can easily be fixed in the ArcInfo GIS environment by using graphical editing tools (ArcEdit). By draping the extracted coastline on the top of the orthorectified SAR images, for instance, incorrect coastline segments for the fast sea ice can be deleted, and new ones can be inserted to close the artificial inlets.

The coastline derived from each image tile was further edited to make all constituent line segments (arcs) be oriented in the counterclockwise direction by flipping the line segments in a clockwise direction in the ArcInfo GIS environment. This facilitates the operations of creating inland buffer zones along the coastline by expanding a certain distance in the left direction and creating seaward buffer zones along the coastline by expanding a certain distance in the right direction. For example, by expanding a distance of 5 km in the left direction, we can create a 5-km coastal zone of the Antarctic continent.

Successive Extraction of Coastline at Two Spatial Resolutions

Our coastline extraction work was performed successively at two spatial resolutions: 100 m and 25 m. First, a series of image tiles was subsetted from the seamless orthorectified SAR image mosaic at a 100-m pixel size along the narrow strip of coastal region. Each image frame has 4096 by 4096 pixels and covers a 409.6-km by 409.6-km ground area, with an overlap of 20 km between adjacent tiles. For the segmentation operation, each image frame was divided into an array of overlapping image blocks, each with 32 by 32 pixels, for determining local threshold values. The vector coastline segments extracted from each image tile were merged into a complete coastline coverage at a 100-m resolution in the ArcInfo GIS environment by using graphical editing tools (ArcEdit).

To obtain the most accurate estimate of the coastline, the second series of image tiles was extracted from the SAR image mosaic at the original resolution of 25 m. Each image tile was then clipped using a 20-km buffer zone along the coastline generated from the 100-m-resolution SAR image tiles. Clipping the image tile aims at reducing image data volume and corresponding computational cost. When processing the 25-m-resolution SAR images, we used the coastline detected from the 100-m SAR images as initial seeds for the image segmentation. The size of the image blocks for bimodal Gaussian curve fitting was expanded to 51 by 51 pixels. Other aspects of the algorithms are similar to those used for processing the 100-m image tiles. The final result is an ArcInfo vector line coverage at a 25-m resolution, which includes the coastlines for the conterminous Antarctic continent and surrounding islands (Figure 7).

Analysis of Antarctic Coastline

The primary component of Antarctic continent is the ice sheet, which is a large mass of glacial ice grounded on the bedrock. The ice sheet deforms and moves with gravity. A ring of flat-topped ice shelves is attached to the ice sheet along one side and floats on continental shelf seas (Figure 2). As noted above, we define the Antarctic coastline as the boundary between ocean and the continental ice sheet, including coastal rock outcrops and ice shelves. It should be noted that our coastline is specific to the September/October 1997 epoch. This is important because Antarctica is one of the few places on Earth where the coastline (ice margin) can change by tens and even hundreds of kilometers in just a few weeks (Scambos *et al.*, 2000).

Resolution, Scale, and Information Content

The relative planimetric fidelity of our SAR-derived coastline is assessed based on a visual comparison between the extracted coastlines and the orthorectified SAR images. By superimposing the extracted coastline on the SAR image mosaic, we carefully inspected all coastline segments with graphical zoom-in, zoom-out, and pan tools in the ArcInfo GIS. The visual examination showed that the extracted coastline closely matched the visual interpretation of the SAR images. The average relative accuracy of coastline position is down to one pixel, namely, within 25 m for the 25-m-resolution coastline coverage. As shown in Figures 6 and 7, subtle coastal features, such as small inlets, headlands, and ice tongues, are accurately delineated. To gain an appreciation of the improvement level over previous efforts, our coastline is compared with the best available digital Antarctic coastline in the Antarctic Digital Database (ADD), which was compiled by the British Antarctic Survey by digitizing a variety of published medium-scale and small-scale maps from many countries (BAS, 1998). The scale of ADD coastline maps ranges from 1:250,000 to 1:1,000,000. The maps at 1:250,000 scale only cover a small portion of the Antarctic coast (mainly over the Antarctic Peninsula and Transantarctic Mountains), and most parts of the Antarctic coastline in the ADD are at a scale of 1:1,000,000. Even compared with the most detailed coastline (1:250,000 scale) in the ADD, our coastline represents a dramatic enhancement in terms of resolution, position, and consistency (Figure 8).

According to the sampling theorem, a 25-m-resolution coastline map is able to detect 50-m or larger coastal features such as inlets, peninsula, and ice tongues. The smallest physical mark that a cartographer can accurately draw on a map is about 0.5 mm (Tobler, 1988), which provides a limit to the smallest features or distance that can be recorded true to scale on a map. Because the 25-m-resolution cell corresponds to 0.5 mm on a 1:50,000-scale map, our coastline derived from 25-m-resolution SAR imagery meets a conventional mapping standard at 1:50,000 scale (Tobler, 1988).

Absolute Accuracy of Planimetric Position

A further problem is whether the "visually correct" coastline derived from the SAR images is geodetically accurate. The absolute positional accuracy of the coastline not only depends on our coastline extraction algorithms but also on the accuracy of the geolocation of the source SAR images. As stated earlier, the absolute geolocation accuracy of SAR image pixels after rigorous orthorectification was estimated at about 50 to 100 m for the SAR image mosaic. This represents the expected average positional accuracy of our coastline product. To validate this expectation, the accuracy of our coastline was assessed by comparing with other independent data sources of higher order. First, several portions of the SAR-derived coastline were compared with those digitized from large-scale (1:5,000 to 1:25,000) topographic maps provided by the Australian Antarctic Division (Lee Belbin and Ursula Ryan, personal communication). Figure 9 shows a small section of these comparisons. The shape of our coastline is consistent with the large-scale topographic map. To quantify the absolute accuracy, we carefully compared 400.4 km of SAR-derived coastline with the coastline in a 1:25,000-scale topographic map of the Vestfold Hills in East Antarctica. This region is dominated by rock outcrops, and therefore the change of the coastline position is minimal. We sampled 7816 points on the SAR-image-derived coastline and computed their distances to

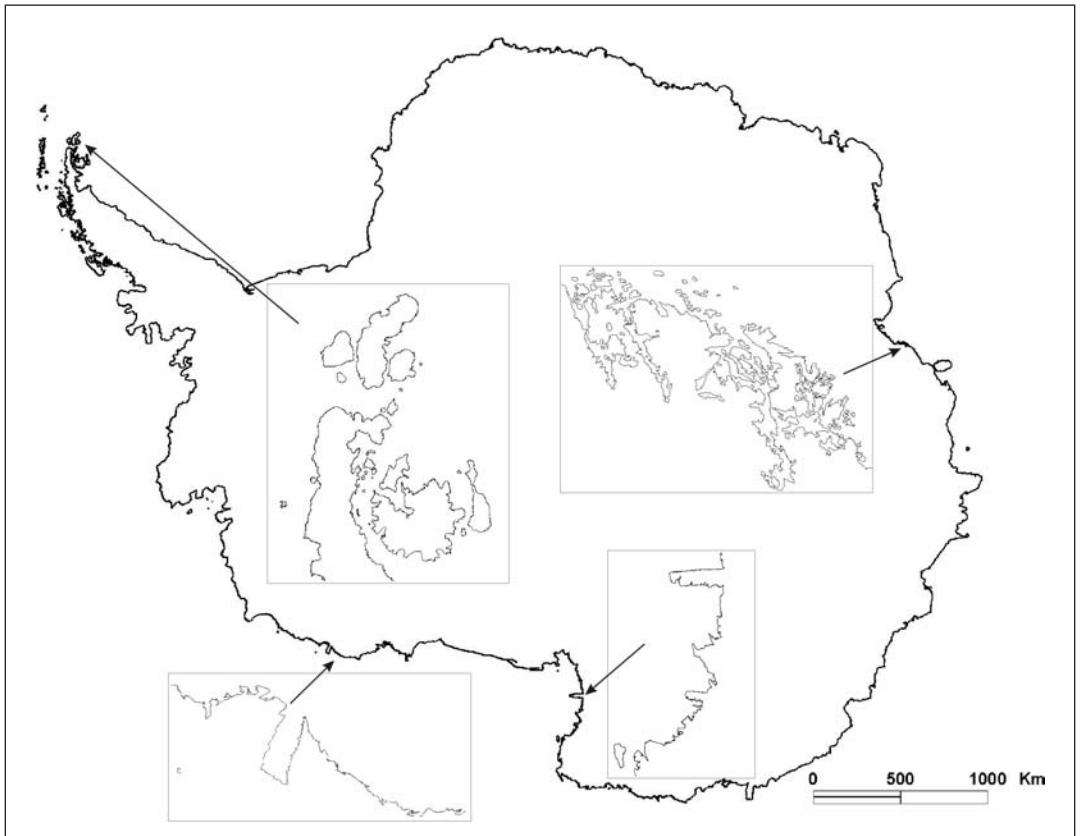

Figure 7. Coastlines of the conterminous Antarctic continent and surrounding islands derived from the 1997 SAR image mosaic.

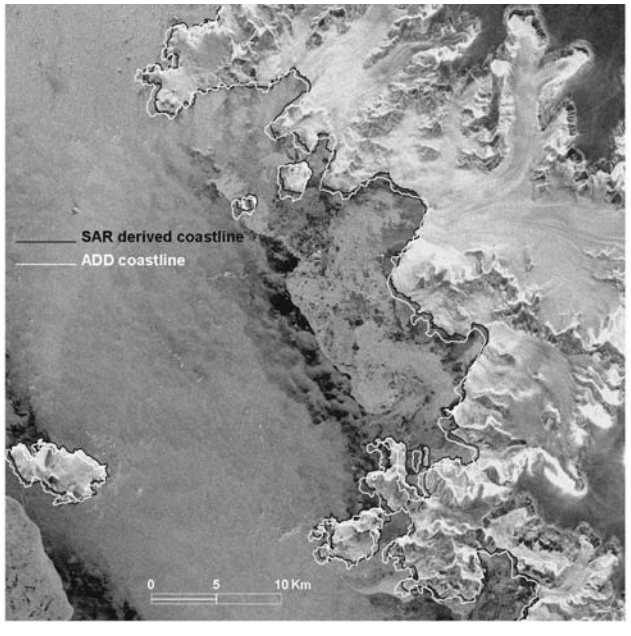

Figure 8. Comparison of the Radarsat SAR-derived coastline with the best available Antarctic coastline (1:250,000 scale) in the Antarctic Digital Database.

the corresponding positions on the topographic map coastline. The mean of the distances is 28.2 m, and the RMSE (root-mean-squared error) is estimated to be 46 m based on the following formula:

$$\mathrm{RMSE} = \sqrt{\frac{\sum_{i=1}^{N} d_i^2}{N}} \tag{14}$$

where d_i is the distance between the SAR-derived coastline and the coastline from the large-scale topographic map at the sample point i, and N is the total number of sampling points.

In addition, our coastline was compared with an orthorectified panchromatic SPOT image in the Dry Valley region. The SPOT image was acquired in 1989 by a pushbroom sensor with a near vertical imaging geometry, and it was precisely geocoded at the USGS. Due to the high spatial resolution (10 m) and the use of many GPS-measured GCPs, the geolocation accuracy of the SPOT image is estimated to be about 10 m (Jean-Claude M. Thomas at the USGS, personal communication). As shown in Figure 10, ice-free rocks dominate the coast of this region. Because the margin of the Ferrar Glacier tongue experienced dynamic change from 1989 through 1997, we conducted the comparison without consideration of this portion of the coastline. With 1478 sampling points along the 52.5-km rock coastline, the mean of the positional differences between the SAR-derived coastline and the SPOT-image-

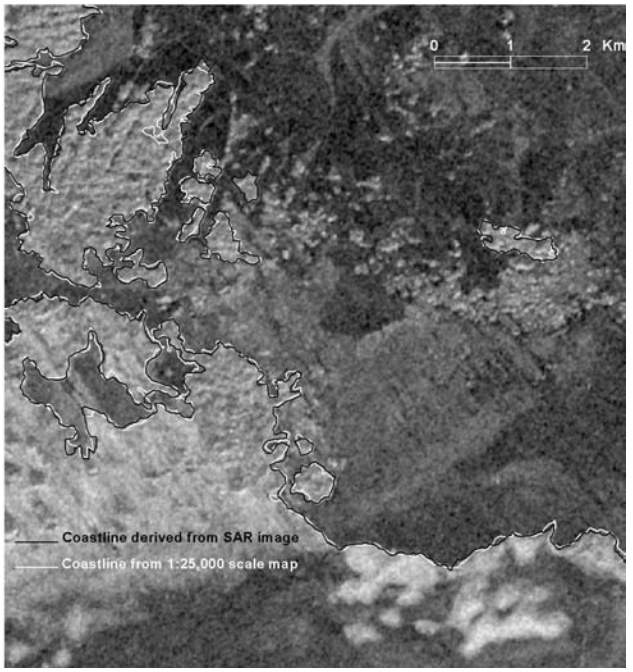

Figure 9. Evaluation of the Radarsat SAR-derived coastlines with reference to a large-scale topographic map (1:25,000).

derived coastline was estimated to be 105.4 m, and the RMSE to be 126.6 m.

Complexity and Shape Property of the Antarctic Coastline

The digital coastline can be used to precisely measure the coastline length and extent of the Antarctic ice sheet (Fox and Cooper, 1994). The length of coastline for the conterminous Antarctic continent is 39,849 km measured from 100-m resolution coastline coverage, and 43,449 km measured from 25-m resolution coastline coverage. The difference between the 100-m and 25-m versions reflects the measurement scale issue that a more detailed map captures more coastal details and hence results in a longer coastline. Our estimate compares with a value of 36,736 km reported by Fox and Cooper based on the 1:1,000,000-scale Antarctic Digital Database (ADD) coastline. To obtain a reliable areal size, the coastline of the conterminous Antarctic continent was projected into the Lambert Azimuth Equal Area map projection. The total area of the Antarctic continent was estimated to be 13,855,857 km^2 from the 100-m resolution coastline map, and 13,855,983 km^2 from the 25-m resolution coastline map (Table 2). This compares with Fox and Cooper's result of 13,949,000 km^2.

We analyzed the inherent irregularity and complexity of the Antarctic coastline using the concept of fractal dimension (Mandelbrot, 1967). A straight line will have a fractal dimension of 1. The more irregular the coastline, the greater the fractal dimension. Highly curved irregular lines will have a fractal dimension close to 2. A walking-divider algorithm (Lam and De Cola, 1993) was used to calculate the fractal dimensions for different parts of the Antarctic coast.

As shown in Table 3, the degree of irregularity of the coastline varies. Differences in the fractal dimension highlight

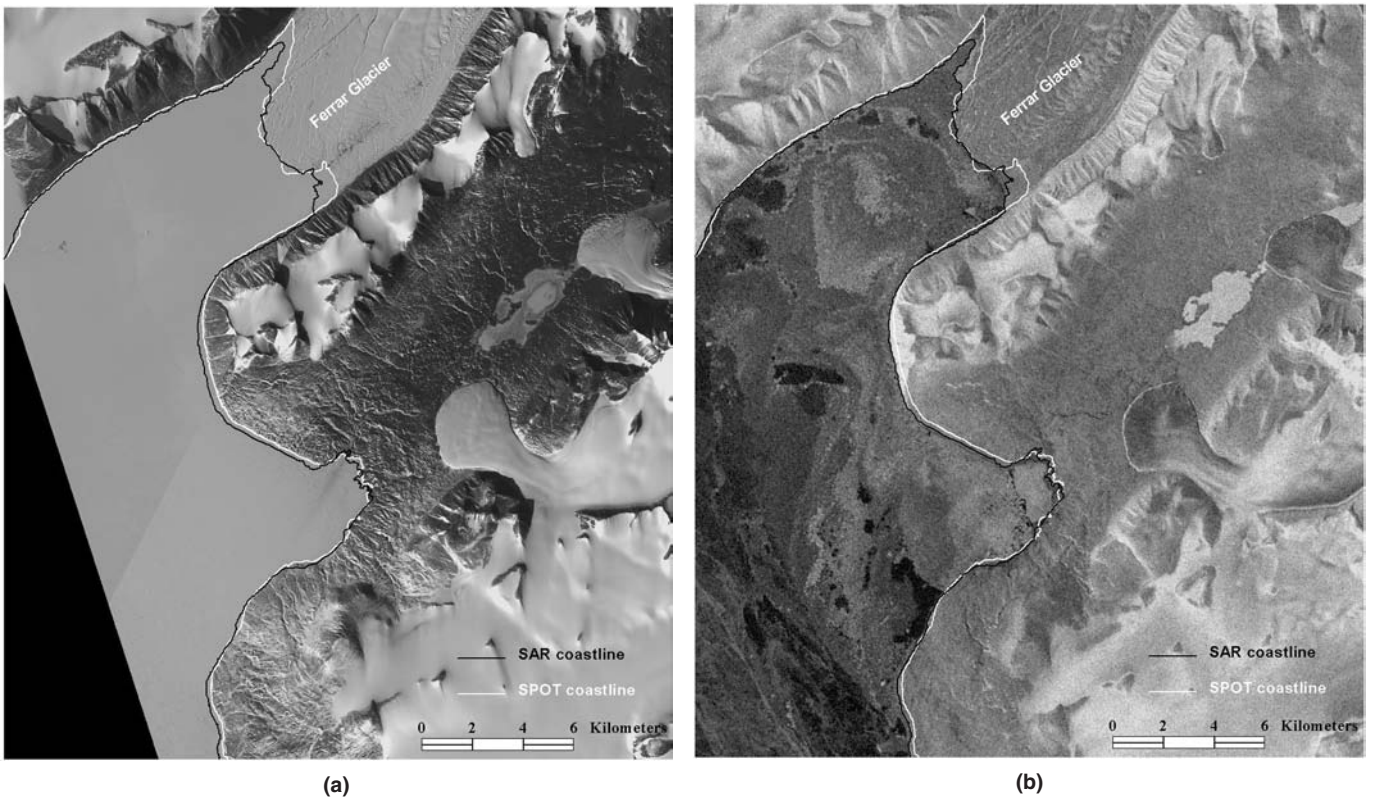

Figure 10. Evaluation of the Radarsat SAR-derived coastline with reference to an orthorectified panchromatic SPOT image (10-m resolution). (a) Draped on the SPOT image. (b) Draped on the SAR image.

the differences in the shape and morphology of the coastline, which in turn reveals the differences in the glaciological and ocean processes acting on the different sections of the Antarctic coast. Coastlines along the Antarctic Peninsula and Victoria Land have the highest fractal dimension, because Alpine (mountain) glacial processes dominate these regions. The coastal regions of Marie Byrd Land, Queen Maud Land, Wilkes Land, and Enderby Land are dominated by small ice shelves or grounded ice sheets, and their coastlines have a moderate fractal dimension. The large ice shelves, including the Ronne Ice Shelf, Filchner-Ronne Ice Shelf, Amery Ice Shelf, and Larsen Ice Shelf, are fed by large and fast ice streams, and their margins (coastlines) are relatively smooth and have no obvious fractal properties.

Conclusions and Future Work

Mapping the Antarctic with the conventional aerial photography method is extremely difficult and costly, due to its remote location, snow and ice covered surface, extremely cold and windy weather condition, and lack of sufficient established geodetic control. Until recently, the Antarctic continent remained poorly charted. Satellite remote sensing technology, especially spaceborne imaging radar, provides an efficient means for mapping the Antarctic. The SAR images acquired by Radarsat-1 in 1997 constitute a near instantaneous, high-resolution view of the entire continent and its offshore ocean, which provides an ideal image source for mapping the Antarctic coastline.

In this research, we developed a comprehensive technique for mapping the Antarctic coastline with satellite radar imagery. Our automated method significantly removed the burden of conventional manual delineation methods. Successful batch processing of a large volume of radar image data demonstrates that our method is effective, robust, and efficient. Our final product is a complete vector map of the Antarctic coastline in ArcInfo line coverage format. It has a spatial resolution of 25 m and meets the standard of the conventional 1:50,000-scale map. Our coastline products are presented in the Polar Stereographic map projection referenced to the WGS84 ellipsoid, which can readily be incorporated into a GIS for supporting a variety of cartographic and scientific applications.

We demonstrated that our coastline captures the unprecedented detail of the Antarctic coastal features. The average relative precision of our coastline is about one pixel, which is extremely difficult to be achieved by the human "on-screen" digitization method. In comparison with independent data sources of higher order, we found that the absolute accuracy of planimetric position of our coastlines may vary from region to region. But the overall accuracy is better than 130 m. We believe that our products represent the most detailed and accurate digital description about the geographic position and geometric shape of the Antarctic coasts published to date.

Our coastline is a nearly instantaneous snapshot of the Antarctic ice sheet margin in 1997, and can serve as a reliable and consistent benchmark for future change-detection studies. In 2000, the entire Antarctic continent was imaged again by the radarsat-1 SAR sensor, and the resulting SAR images are being processed for orthorectification at Byrd Polar Research Center. Our coastline extraction method will be used to extract the 2000 Antarctic coastline. In addition, Kim *et al.* (2001) have produced an image mosaic based on the Declassified Intelligence Satellite Photographs (DISP) collected in the 1960s. Sequential mapping of ice sheet margins provides a simple and direct method for measuring the extent and velocity of ice sheet advance or retreat in the Antarctic coasts that have occurred over the past four decades.

TABLE 2. RESOLUTION, SCALES, AND INFORMATION CONTENT OF ANTARCTIC COASTLINE PRODUCTS

Parameters	Product I	Product II
Resolution	100 m	25 m
Scale	1:200,000	1:50,000
Detectable features	200 m	50 m
File format	ArcInfo line coverage	ArcInfo line coverage
Measured length	39,849 km	43,449 km
Measured Area	13,855,857 km^2	13,855,983 km^2

TABLE 3. FRACTAL DIMENSIONS OF ANTARCTIC COASTS (LOCATIONS ARE SHOWN IN FIGURE 2). R IS THE CORRELATION COEFFICIENT FOR THE LINEAR REGRESSION EQUATION FITTED ON THE LOG-LOG RICHARDSON PLOT

Coastline Location	Fractal Dimension (D)	Correlation Coefficient (R)
Antarctic Peninsula	1.144161	0.919570
Victoria Land	1.132256	0.952279
Enderby Land	1.112726	0.975695
Queen Maud Land	1.112708	0.930209
Marie Byrd Land	1.103373	0.959526
Wilkes Land	1.074653	0.983909
Amery Ice Shelf	1.070313	0.971222
Larsen Ice Shelf	1.048531	0.974735
Filchner-Ronne Ice Shelf	1.048647	0.932743
Ross Ice Shelf	1.047904	0.919942
Entire Antarctica	1.096448	0.959921

Acknowledgments

This work was supported by NASA grant NAG5-10112 and NSF grant No. 0126149. SAR data were processed and provided by the Radarsat: Antarctic Mapping Project of the Byrd Polar Research Center. The authors would like to thank Katy Noltimer for identifying and extracting coastal image tiles from the image database, Jean-Claude Thomas for providing the SPOT image for the Dry Valley region, Lee Belbin and Ursula Ryan for providing several digitized large-scale topographic maps, and Biyan Li for editing and merging the coastline.

References

BAS (British Antarctic Survey), 1998. *Antarctic Digital Database: Manual and Bibliography Version 2.0*, Scientific Committee on Antarctic Research, Cambridge, United Kingdom, 74 p.

Canny, J., 1986. A computational approach to edge detection. *IEEE Transactions on Pattern Analysis and Machine Intelligence*, 8(6):679–698.

Chow, C.K., and T. Kaneko, 1972. Automatic boundary detection of the left ventricle from cineagiograms, *Computer and Biomedical Research*, 5:388–410.

Curlander, J.C., R. Kwok, and S. Pang, 1987. A post-processing system for automated rectification and registration of spaceborne SAR imagery, *International Journal of Remote Sensing*, 8(4):621–638.

Ferrigno, J., J. Mullins, J. Stapleton, P. Chavez, Jr., M. Velasco, R. Williams, Jr., G. Delinski, Jr., and D. Lear, 1996. *Satellite Image Map of Antarctica*, Miscellaneous Investigations Series, Map 1–2560, U.S. Geological Survey, Reston, Virginia.

Fox, A.J., and A.P. Cooper, 1994. Measured properties of the Antarctic ice sheet derived from the SCAR Antarctic digital database, *Polar Record*, 30(174):201–206.

Haverkamp, D., L.K. Soh, and C. Tsatsoulis, 1995. A comprehensive, automated approach to determining sea ice thickness from SAR data, *IEEE Treansactions on Geoscience and Remote Sensing*, 33(1):46–57.

Jezek, K.C., 1999. Glaciologic properties of the Antarctic Ice Sheet from spaceborne synthetic aperture radar observations, *Annals of Glaciology*, 29:286–290.

———, 2002. Radarsat-1 Antarctic Mapping Project: Change detection and surface velocity campaign, *Annals of Glaciology*, 34:263–268.

Jezek, K.C., and F.D. Carsey, 1993. *Radarsat: The Antarctic Mapping Project*, Report No. 6, Byrd Polar Research Center, The Ohio State University, Columbus, Ohio, 24 p.

Jezek, K., H. Liu, Z. Zhao, and B. Li, 2000. Improving Antarctic digital elevation model by using radar remote sensing and GIS techniques, *Polar Geography*, 23(3):209–224.

Johnsen, H., L. Lauknes, and T. Guneriussen, 1995. Geocoding of fast-delivery ERS-1 SAR image mode product using DEM data, *International Journal of Remote Sensing*, 16(11):1957–1968.

Kim, K., K.C. Jezek, and H.G. Sohn, 2001. Ice shelf advance and retreat rates along the coast of Queen Maud Land, Antarctica, *Journal of Geophysical Research*, 106(C4):7097–7106.

Kwok, R., J.C. Curlander, and S. Pang, 1990. An automated system for mosaicking spaceborne SAR imagery, *International Journal of Remote Sensing*, 11(2):209–223.

Lam, Nina Siu-Ngan, and Lee De Cola, 1993. Fractal measurement, *Fractals in Geography* (Nina Siu-Ngan Lam and Lee De Cola, editors), Prentice Hall, Inc., Englewood Cliffs, New Jersey, pp. 23–55.

Larsgaard, M.L., 1993. *Topographic Mapping of Africa, Antarctica, and Eurasia*, Occasional Paper No. 14, Western Association of Map Libraries, Santa Cruz, California, 264 p.

Leberl, F.W., 1990. *Radargrammetric Image Processing*, Artech House, Inc., Norwood, Massachuesetts, 593 p.

Lee, J.S., 1986. Speckle suppression and analysis for synthetic aperture radar images, *Optical Engineering,* 25(5):636–643.

Lee, J.S., and I. Jurkevich, 1990. Coastline detection and tracing in SAR images, *IEEE Transactions on Geoscience and Remote Sensing,* 28:662–668.

Liu, H., K. Jezek, and B. Li, 1999. Development of Antarctic Digital Elevation Model by integrating cartographic and remotely sensed data: A GIS-based approach, *Journal of Geophysical Research*, 104(B10):23,199–23,213.

Liu, H., and K. Jezek, 2004. Automated extraction of coastline from a satellite imagery by integrating Canny edge detection and locally adaptive thresholding methods, *International Journal of Remote Sensing*, 25(5):937–958.

Mandelbrot, B.B., 1967. How long is the coast of Britain? Statistical self-similarity and fractional dimension, *Science*, 156:636–638.

Mason, D.C., and I.J. Davenport, 1996. Accurate and efficient determination of the shoreline in ERS-1 SAR Images, *IEEE Transactions on Geoscience and Remote Sensing,* 34:1243–1253.

Mercer, J., 1978. West Antarctic ice sheet and CO2 greenhouse effect: A threat of disaster, *Nature*, 271(5643):321–325.

Mullins, J.L., C.A. Hallam, L.D. Hothem, and J.-C. Thomas, 1999. The geodesy and mapping program of the United States Geological Survey in Antarctica, *Photogrammetric Engineering & Remote Sensing*, 65(12):1340–1341.

Naraghi, M., W. Stromberg, and M. Daily, 1983. Geometric rectificastion of radar imagery using digital elevation models, *Photogrammetric Engineering & Remote Sensing*, 49(2):195–199.

Norikane, L., B. Wilson, and K.C. Jezek, 1996. RADARSAT Antarctica mapping system: System overview, *Proceedings IGARSS'96*, 21–26 May, Lincoln, Nebraska (IEEE), pp. 1772–1774.

Parker, J.R., 1997. *Algorithms for Image Processing and Computer Vision*, John Wiley & Sons, Inc., New York, N.Y., 417 p.

Perona, P., and J. Malik, 1990. Scale-space and edge detection using anisotropic diffusion, *IEEE Transactions on Pattern Analysis and Machine Intelligence*, 12:629–639.

Press, W.H., S.A. Teukolsky, W. T. Vetterling, and B.P. Flannery, 1992. *Numerical Recipes in C: The Art of Scientific Computing*, Cambridge University Press, Cambridge, United Kingdom, 1002 p.

Ryan, T.W., P.J. Sementilli, P. Yuen, and B.R. Hunt, 1991. Extraction of shoreline features by neural nets and image processing, *Photogrammetric Engineering & Remote Sensing*, 57:947–955.

Saint-Marc, P., J. Chen, and G. Medioni, 1991. Adaptive smoothing: A general tool for early vision, *IEEE Transactions on Pattern Analysis and Machine Intelligence*, 13:514–529.

Scambos, T.A., C. Hulbe, M.A. Fahnestock, and J. Bohlander, 2000. The link between climate warming and breakup of ice shelves in the Antarctic Peninsula, *Journal of Glaciology*, 46(154):516–530.

Sohn, H.G., and K.C. Jezek, 1999. Mapping ice sheet margins from ERS-1 SAR and SPOT imagery, *International Journal of Remote Sensing*, 20:3201–3216.

Swithinbank, C., 1988. *Satellite Image Atlas of Glaciers of the World: Antarctica*, Professional Paper 1386-B, United States Geological Survey, U.S. Government Printing Office, Washington, D.C., 278 p.

Tobler, W., 1988. Resolution, resampling, and all that, *Building Databases for Global Science* (H. Mounsey, and R. Tomlinson, editors), Taylor and Francis, New York, N.Y., pp. 129–137.

Williams, R.S., Jr., and D.K. Hall, 1993. Glaciers, *Atlas of Satellite Observations Related to Global Change* (R.J. Gurney, J.L. Foster and C.L. Parkinson, editors), Cambridge University Press, Cambridge, United Kingdom, pp. 401–422.

Williams, R.S., Jr., J.G. Ferrigno, C. Swithinbank, B.K. Lucchitta, and B.A. Seekins, 1995. Coastal change and glaciological maps of Antarctica, *Annals of Glaciology*, 21:284–290.

(Received 03 January 2003; accepted 13 April 2003; revised 23 May 2003)